Facile Synthesis and Phase Stability of Cu-based Na 2 Cu(SO 4) 2 .xH 2 O (x = 0-2) Sulfate Minerals as Conversion type Battery Electrodes

Shashwat Singh, Audric Neveu, K. Jayanthi, Tisita Das, Sudip Chakraborty, Alexandra Navrotsky, Valérie Pralong, Prabeer Barpanda

Facile Synthesis and Phase Stability of Cu-based $Na_2Cu(SO_4)_2.xH_2O$ (x = 0-2) Sulfate Minerals as Conversion type Battery Electrodes

Shashwat Singh,†# Audric Neveu,# K. Jayanthi,$ Tisita Das,‡ Sudip Chakraborty,‡ Alexandra Navrotsky,$ Valérie Pralong,# and Prabeer Barpanda†§*

† Faraday Materials Laboratory (FaMaL), Materials Research Center, Indian Institute of Science, Bangalore 560012, India

Normandie University, ENSICAEN, UNICAEN, CNRS, CRISMAT, 14000 Caen, France

$ School of Molecular Sciences and Navrotsky Eyring Center for Materials of the Universe, Arizona State University, Tempe, Arizona 85287, United States

‡ Materials Theory for Energy Scavenging (MATES) Lab, Harish-Chandra Research Institute (HRI), HBNI, Chhatnag Road, Jhunsi, Prayagraj 211019, India

§ Helmholtz Institute Ulm (HIU), Helmholtzstraße, Ulm 89081, Germany

Corresponding Author

*E-mail: prabeer@iisc.ac.in

ABSTRACT

Mineral exploration forms a key approach to unveil functional battery electrode materials. Synthetic preparation of naturally found minerals and their derivatives can aid in design of new electrodes. Herein, saranchinaite $Na_2Cu(SO_4)_2$ and its hydrated derivative kröhnkite $Na_2Cu(SO_4)_2.2H_2O$ bisulfate minerals have been prepared using a facile spray drying route for the first time. The phase stability relation during (de)hydration process was examined synergising *in-situ* X-ray diffraction and thermochemical studies. Kröhnkite forms the thermodynamically stable phase as the hydration of saranchinaite to kröhnkite is highly exothermic (-51.51 ± 0.63 KJ/mol). Structurally, kröhnkite offers a facile 2D pathways for Na^+ ion migration resulting in 20 times higher total conductivity than saranchinaite at 60 °C. Both compounds exhibited conversion redox mechanism for Li-ion storage with first discharge capacity exceeding 650 mAh/g (at 2 mA/g *vs.* Li^+/Li) upon discharge up to 0.05 V. *Post-mortem* analysis revealed the presence of metallic Cu in the discharged state is responsible for high irreversibility during galvanostatic cycling. This study reaffirms the exploration of Cu-based polyanionic sulfates, while having limited (de)insertion property, can be harnessed for conversion-based electrode materials for batteries.

TOC

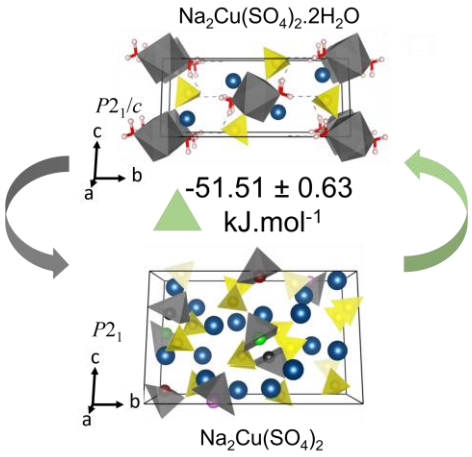

INTRODUCTION

Naturally occurring minerals form a rich database of compounds investigated for their diverse crystal chemistry and variety of functional applications. Polyanionic materials form a sub-class of such minerals, which exhibit insertion or conversion reaction based battery chemistry. Indeed, alkali-ion (de)insertion chemistry has been observed in polyanionic minerals such as Fe_2SiO_4 (fayalite), $LiFePO_4$ (triphylite), $LiFe_{1-x}PO_4$ (laihunite $Fe_{2-x}SiO_4$), $LiFeSO_4F$ (triplite $(Mn,Fe,Ca)_2PO_4(OH,F)$)[1], $LiVPO_4F$ (tavorite $LiFePO_4OH$), and $FePO_4.2H_2O$ (phosphosiderite).[2,3] Polyanionic minerals having sulfate groups (polyanionic sulfates) are particularly interesting as they offer rich crystal chemistry and high redox potential of the transition metal based on the 'inductive effect' stemming from higher electronegativity of sulfate [SO_4^{2-}] units.[4] Following, the electrochemical properties of several mineral inspired polyanionic sulfates as electrodes have been reported such as alluaudite $Na_{2+2x}Fe_{2-x}(SO_4)_3$[5], eldfellite-yavapaiite $AFe(SO_4)_2$ (A = Na, K)[6–8] etc.

Given the similarity (~ 0.17 v.u.) between the Lewis basicity of O atoms in sulfate SO_4^{2-} and H_2O, the anhydrous polyanionic sulfates are generally unstable in ambient conditions. In such context, the mechanistic insight of (de)hydration process and the interplay of phase stability becomes important for a tight control over the material processing parameters. The reversibility

of (de)hydration process offers utilization of energy of hydration for thermochemical energy storage. For instance, *saranchinaite* $Na_2Cu(SO_4)_2$ (Cu-src) and its hydrated analogue kröhnkite $Na_2Cu(SO_4)_2.2H_2O$ (Cu-krh) were reported as a pair of polyanionic bisulfate salts having an excellent (76.6 %) reversibility of (de)hydration process, thereby serving as candidate for sustainable thermochemical energy storage.[9,10] Various hydrated sulfates $Na_2M(SO_4)_2.xH_2O$ (x = 2, kröhnkite and x = 4, blöedite) have been reported as suitable insertion hosts.[11,12] However, their electrochemical performance is hampered owing to the dead mass of structural water and reactivity with the electrolyte. Recently, on electrochemical front, Cu-*src* delivered limited (dis)charge capacity based on (de)insertion reaction due to the absence of ionic migration channels and higher redox potential of Cu^{3+}/Cu^{2+} (Jahn-Teller active) redox couple.[13,14] Such compounds, devoid of ionic channels, have been found to exhibit conversion reaction in the lower voltage range (0-3 V) utilizing multiple oxidation state of the transition metal ($T_M^{n+} \rightarrow T_M^0$), delivering high gravimetric capacity. However, the conversion reaction proceeds with chemical transformation of the pristine compound involving the extrusion of T_M and formation of by-products (AF, A_2O, A_2S, A_2SO_4 etc. | A = Li, Na, K) accompanied by large volume change. Consequently, conversion chemistry often suffers from poor reversibility.[14–20]Among analogous T_M based compounds, the lower formation (less negative) energy of Cu-based materials can theoretically yield higher redox potential during conversion reaction.[21]

In this context, the conversion chemistry of various Cu-based polyanionic sulfates have been reported such as $CuSO_4$[18], bronchantite $Cu_4(OH)_6SO_4$)[20], and $Li_2Cu_2O(SO_4)_2$[14]. Following Cu chemistry, we have revisited $Na_2Cu(SO_4)_2.xH_2O$ (x = 0-2) bisulfates with facile spray drying synthesis. The dynamics of (de)hydration step, saranchinaite ↔ krohnkite phase transformation, and phase stability have been investigated by synergistic analysis of *in situ* techniques

(thermodiffraction and hydration) and thermochemistry. The electronic properties and ionic conductivity have been analysed using experimental and computational tools. Following, the conversion chemistry of these Cu-based materials have been tested for reversible Li ion storage.

EXPERIMENTAL

Synthesis of *Saranchinite* $Na_2Cu(SO_4)_2$. The target phase was obtained using a two-step spray drying route. The intermediate phase was prepared using spray drying synthesis (SDS) route, using Büchi B-90 spray dryer, from a homogeneous aqueous precursor solution having stoichiometric amounts of Na_2SO_4 (SDFCL, 99.5%) and $CuSO_4.5H_2O$ (SDFCL, 99%). The nebulized droplets during spray drying instantly dried while descending the chamber having fixed inlet (220 °C) and outlet (80 °C) temperature. Aqueous medium and water soluble SO_4-precursors led to intimate mixing and facile ionic diffusion vis-à-vis solid-state route. In the first step of SDS, formation of an intermediate complex occurred as the feed precursor solution and hot gas entered the spray drying chamber in the co-current mode. In the second step, the intermediate complex powder was annealed in the temperature range of 250-400 °C for 0.5-2 h in ambient condition. The use of aqueous medium allows direct use of hydrated precursors ($CuSO_4.5H_2O$), demanding less stringent storage conditions thereby making SDS economic and scalable. Further details on the SDS route is reported elsewhere.[22]

Synthesis of *Kröhnkite* $Na_2Cu(SO_4)_2.2H_2O$. The target compound was prepared via a classical dissolution-precipitation route. First, equimolar quantities of Na_2SO_4 (SDFCL, 99.5%) and $CuSO_4 \cdot 5H_2O$ (SDFCL, 99%) precursors were dissolved in a minimal amount of distilled water. Following, ethanol was added to this precursor solution in (2:1) ratio to precipitate the kröhnkite

(Cu-krh) phase. This precipitate was recovered by centrifuging and was dried in a vacuum chamber at 60 °C for 12 h. Alternatively, the kröhnkite phase can be derived by hydration of saranchinite phase in a controlled humidity chamber as well as in ambient atmosphere.

Structural and Physical Analysis. Powder X-ray diffraction (PXRD) patterns were acquired using PANalytical Empyrean X-ray diffractometer (PANanalytical, Malvern, UK) having Cu-Kα source (λ_1 = 1.5405 Å, λ_2 =1.5443 Å) operating at 40 kV/30 mA. PXRD patterns were collected in Bragg-Brentano geometry (reflection mode) in the 2θ range of 10-80° with a step size of 0.026°. Rietveld refinement was performed with the ED-PCR program embedded in FullProf suite.[23] Crystal structures were illustrated using VESTA software.[24]

The powder morphology was observed using a Carl Zeiss Ultra55 Field Emission Scanning Electron Microscope (FESEM), having a thermal field emission type tungsten source operating at 0.1-30 kV. The powder samples were gold sputtered to avoid charging during interaction with electron beam. The spatial elemental distribution was examined at 10 kV in both line scan and area scan mode using an Energy selective Backscattered (EsB) detector.

A Bruker D8 Advanced diffractometer (Karlsruhe, Germany) (Cu $K\alpha_1$, λ=1.5418 Å), operating in reflection geometry mode, was used to observe the phase evolution during hydration of saranchinaite to kröhnkite in a controlled relative humidity (RH ~60-90 %) using an Anton Paar CHC plus humidity chamber (Graz, Austria). Thermodiffraction study was conducted using a Rigaku SmartLab diffractometer equipped with rotating anode (45 kV, 200 mA) with Cu source (Kα1/α2 = 0.4970) operating in Bragg-Brentano geometry. Corresponding diffractograms were acquired at different temperatures (RT-600 °C, interval = 20 °C, heating rate = 5 °C/min) by attaching an Anton Paar HTK1200N thermal chamber (Graz, Austria).

Isothermal Acid Solution Calorimetry. Dissolution enthalpy of saranchiniate and Cu-Kröhnkite was measured using both CSC 4400 isothermal (with IMC data acquisition software) and Hart Scientific (with Labview software) microcalorimeters with mechanical stirring of the samples and reagents at 25 °C. Calorimeters were calibrated with KCl (NIST standard reference material) by dissolving 15 mg pellets in 25 g of water (at 25 °C). The solution enthalpy of this reference concentration (0.008 mol kg^{-1}), as deduced from the literature, and enthalpy of dilution measurements were used to arrive at the calorimeter calibration factor.[25]

In a typical calorimetry test, 6–8 mg of sample was pressed into a pellet and then dropped into 25 g of 5M HCl placed in the sample chamber of the calorimeter as mentioned elsewhere[22,36]. The sample dissolution causes the heat flow due to temperature difference and is recorded as a calorimetric signal. The integrated area under the recorded microwatt signal from a linear baseline corresponds to total heat effects, which on conversion into joules with KCl calibration corresponds to the enthalpy of sample dissolution (ΔH_{ds}). An appropriate thermochemical cycle based on Hess' law was used to calculate the enthalpy of formation. All the samples dissolve in 5N HCl to form dilute solutions containing dissolved sodium, copper, and sulfate ions and water. X-ray diffraction and thermal analysis (TG-DSC) were performed before and after the calorimetric measurement to detect any possible decomposition and check for adsorbed water on the sample due to the exposure in the ambient atmosphere.

Impedance Measurement. Ionic conductivity of pellets was measured using AC impedance spectroscopy. The pristine powder was pelletized uniaxially (ϕ =10 mm, t = 0.1 cm) under 200

MPa. Further compaction was achieved by isostatic pressing at ~900 MPa resulting in final relative density (ρ_{exp}/ρ_{true}) in the range of 80-90 %. Both sides of these pressed pellets were gold coated to serve as electrical contacts while inhibiting the ionic exchange from the surface. AC impedance spectra were acquired using frequency response analyzer (Solartron, 1260) with a voltage excitation of 500 mV (amplitude) in the frequency range of 0.1 Hz– 1 MHz in the temperature range of RT–300 °C. These spectra were analyzed using BT Lab software.

Electrochemical Characterization. The pristine powder was milled with Super P® carbon (80:20) using Spex® 8000M miller for 30 minutes (10×3 minutes, 10 min intermittent rest). Polytetrafluorethylene (PTFE-Fluka) binder was added into this mixture to obtain the final active material/ Super P Carbon/ binder ratio of 70/20/10. Following, this mixture was rolled into thin sheets acting as working electrodes. Half-cells (2032-type and Swagelok®- cell) were assembled in Ar-filled glove box (MBraun GmbH, 3 mbar, O_2 and H_2O <5 ppm) with configuration: cathode | glass fiber separator soaked with 1M $LiClO_4$ dissolved in propylene carbonate (PC) acting as electrolyte | Li metal foil (as counter and reference electrode). These cells were characterized using Neware® BTS-4000A and BioLogic® BCS-805/810 workstations.

The phase evolution along with variation in oxidation states during conversion reaction were inspected using *ex situ* XRD and X-ray photoelectron spectroscopy (XPS). Swagelok® cells, disconnected at different voltages during cycling, were dissembled in Ar-filled glove box. The recovered cathode sheets were washed with anhydrous dimethyl carbonate (DMC) solvent, dried, and tightly packed in sample vial before further characterization. The XPS spectra were corrected with respect to graphitic C (284.5 eV) peak position and subsequently fitted using CasaXPS software using Shirley background and Gaussian (30)-Lorentzian (70) line shape function.

***Ab-initio* Calculations.** To gauge the electronic properties of saranchinaite $Na_2Cu(SO_4)_2$, the projected density of states (PDOS) and band gap in both full and half-desodiated system were calculated through first principles density functional theory (DFT) calculations.[26] The DFT calculations were performed using Projector Augmented Wave (PAW) method[27] as implemented in Vienna *Ab initio* Simulation Package (VASP) [28] with a converged kinetic energy cut-off of 500 eV. Throughout the calculations, the exchange-correlation functional was approximated using Perdew-Burke-Ernzerhof (PBE) type generalized gradient approximation (GGA). [29] In order to find the minimum energy configuration, all of the structures were fully relaxed until the Hellman−Feynman forces of the constituent atoms became smaller than 0.01 eV/ Å, while self-consistency was achieved with a 0.001 eV convergence accuracy. 5×3×5 Monkhorst-Pack k-points grid was used to sample the Brillouin zone during geometry optimization and total energy calculation.[30]

RESULTS AND DISCUSSION

Synthesis and structural analysis. The metallic bisulfates class of minerals with general formula $AT_M(SO_4)_2.xH_2O$ (A= Li, Na, K; T_M= transition metal; x=0-6) are known to exhibit rich crystal chemistry, polymorphism and high voltage (de)insertion chemistry for alkali ion batteries.[7,8,11–13,31,32] It is noted that based on the synthesis routes, either stable mineralogical phase (high energy route) or new metastable phases (low energy, soft chemistry routes) can be prepared. Indeed, the metastable monoclinic $Li_2Ni(SO_4)_2$ was reported using spray drying synthesis (SDS) route.[22] Additional factors such as presence of the Jahn-Teller active cation (e.g. Mn^{2+}, Cu^{2+}) may further introduce a metastability factor in the phase stability of materials. In this pursuit, SDS route was employed to prepare Cu-src and its hydrated analogue Cu-krh. The SDS route proceeds with formation of an intimate mixture of hydrated precursors in aqueous solution

followed by rapid dehydration in the drying chamber column to yield an intermediate complex. The XRD pattern of this complex did not match with hydrated compounds from Na_2SO_4-$CuSO_4$-H_2O system and precursors such as $CuSO_4.5H_2O$, $Na_2SO_4.10H_2O$, *poitevinite* $CuSO_4.H_2O$ and *thenardite* Na_2SO_4 (Fig. S1). The thermal analysis of the intermediate complex revealed three endothermic peaks with onset temperature at 176 °C, 504 °C and 533 °C (Fig. S2). The weight change of ~10.65 % related to first endothermic peak is equivalent to the loss of nearly 2 moles of H_2O. The second and third endothermic peaks correspond to *puninite* $Na_2Cu_3O(SO_4)_3$ formation and melting, respectively. The exothermic peak observed during cooling indicates melt recrystallisation.[13]

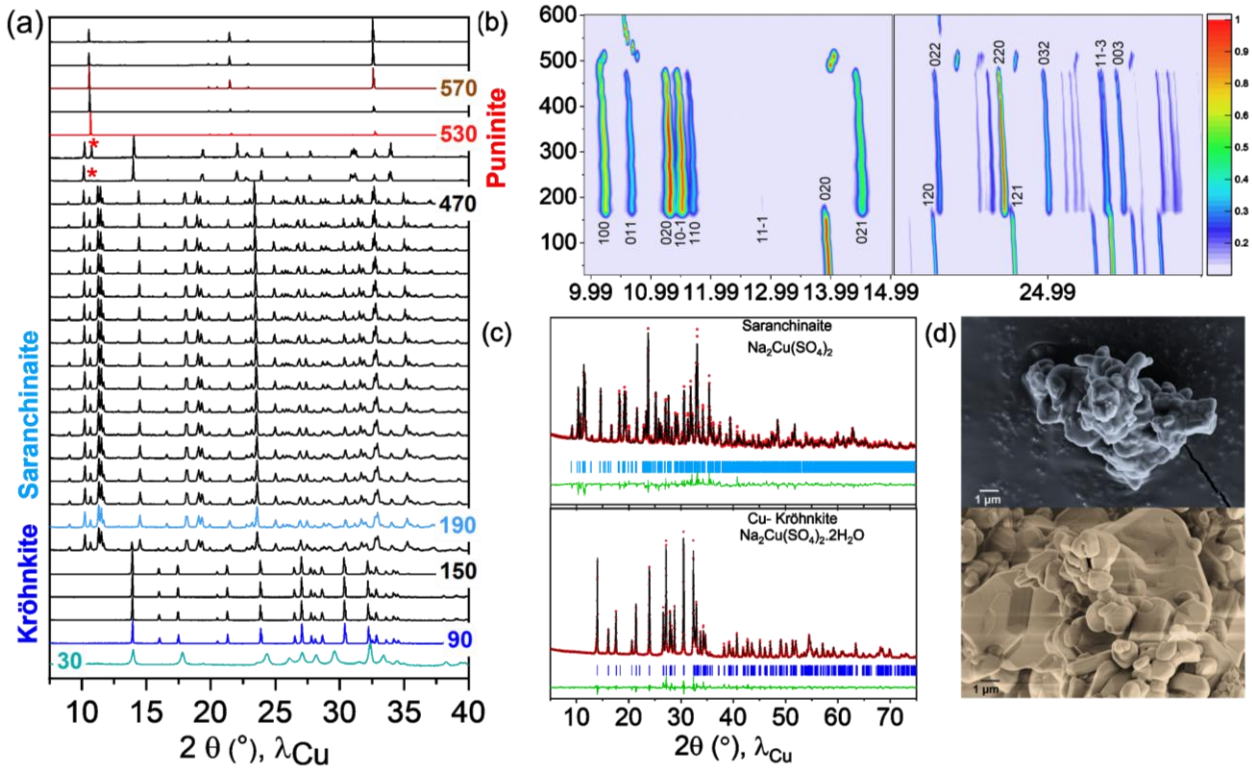

Fig. 1 Dehydration behavior. (a) *In-situ* thermodiffraction plot of spray dried intermediate complex of $Na_2Cu(SO_4)_2$. The thermodiffraction was acquired in the temperature range of 30-600 °C at a temperature interval of 20 °C (@5 °C/min, air). (b) Magnified region of the *in-situ* thermodiffration plot in the 2θ range (left) 10-15° and (right) 20-30°. Cu-krh is stable up to 150 °C followed by an intermediate region of mixed phase assembly with Cu-src up to 470 °C. (c)

Rietveld plot of Cu-src (top) and Cu-krh (bottom). (d) Representative electron microscopy image of Cu-src (top) and Cu-krh (bottom).

Based on thermal analysis, the intermediate complex could have a low temperature metastable phase having 2 moles of structural water. The corresponding temperature dependent phase evolution (in air) was captured by *in-situ* thermodiffraction plot (Fig. 1a). With increase in temperature from 30 °C (bottom), the intermediate phase rapidly transformed to kröhnkite phase having stability up to 150 °C. Further increase in temperature resulted in the dehydration of kröhnkite accompanied with the formation of saranchinaite phase at 170 °C, which was stable in the temperature range of 190-470 °C. At 490 °C, formation of an unknown phase along with minority puninite (red *) $Na_2Cu_3O(SO_4)_3$ phase[33] was observed. The puninite phase dominates upon heating at 530 °C. Following, it melted at 570 °C resulting in growth of characteristic XRD peaks corresponding to the assembly of melt products: Na_2SO_4 (thenardite), CuO (tenorite) along with an unknown phase. The phase evolution of kröhnkite up to 600 °C is in sync with previous report.[9,13] On cooling, recrystallisation of puninite would occur as per exothermic peak observed in the thermal analysis (Figure S2). For clarity, the magnified regions of thermodiffraction plot in the 2θ range of 10-15° (left) and 20-30°(right) are presented as contours in Fig. 1b. Overall, a gradual shift of the XRD contours towards lower 2θ angle is observed for both Cu-krh and Cu-src phases implying thermal expansion of the unit cell. Both phases undergo anisotropic thermal expansion.[9] Rietveld plots of Cu-krh (s.g. $P2_1/c$, #14) and Cu-src ($P2_1$, #4) phases are shown in Fig. 1c. The corresponding lattice and atomic parameters are provided in Table S1 and S2, respectively. The Cu-krh was observed as agglomerates having primary particles of the order of 1-2 μm with sharp features (Fig. 1d). Such morphology is typical of products obtained from dissolution precipitation route, which can also occur due to supersaturation during the facile

spray drying process. In comparison, Cu-src powder had smaller agglomerates with diffused features possibly arising from the breakage of pristine particles during dehydration step.

The enthalpy of hydration of Cu-krh can be utilized for thermochemical energy storage with efficiency of 76.6 % at a charge temperature of 167 °C.[10] This high efficiency stems from high reversibility of the (de)hydration process between Cu-krh and Cu-src phases with minimal structural degradation. It was examined using an *in-situ* XRD equipped with a humidity-controlled chamber. As shown in Fig. 2a, at a relative humidity (RH) of 70% for 1.5 h, the pristine Cu-src began to hydrate as indicated by the appearance of characteristic Cu-krh peak near 14° Bragg angle (marked #). A small XRD peak of Cu-src (marked *) can be still seen at 23.64° after 16 h (at RH 70 %). In the next 5 h at 87 % RH, the growth of Cu-krh phase continued. No further change in the XRD pattern marked the completion of hydration process. Overall, the hydration reaction front appears to proceed from the surface to bulk (shell-core) of the powder[34] and progressively become slower since kröhnkite peaks were initially identified in 1.15 h but took another 20 h to grow fully. The absence of any intermediate hydrates underscores the mirroring of the mechanism of dehydration. Structurally, the two phases are completely unrelated. This is attributed to the polyhedral distortion due to the presence of Jahn-Teller active Cu^{2+} cation, which becomes pronounced during dehydration.[13] The unit cells of both Cu-src and Cu-krh end-members, projected along *a* axis, are illustrated in Figure 2(b, c), respectively.

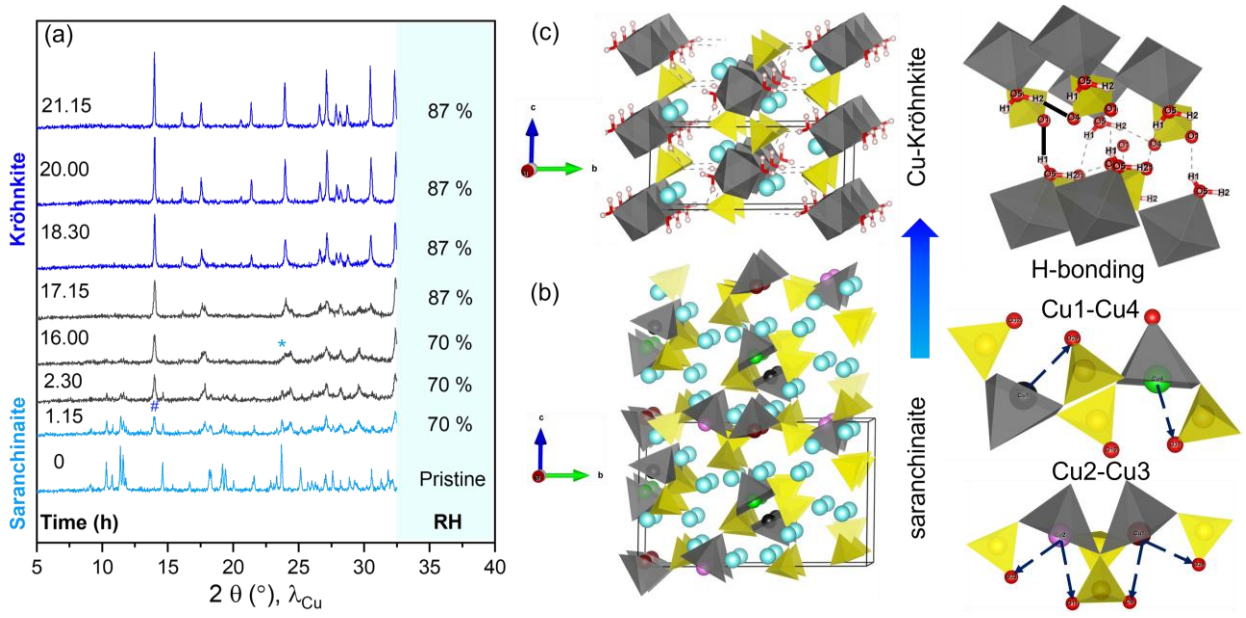

Fig. 2 Hydration behavior. (a) *In-situ* XRD plot obtained during hydration of pristine Cu-src synthesized by heat treatment of spray dried intermediate complex at 405 °C- 0.5 h (air). The characteristic peaks of Cu-src fade at about 2.5 h at 70 % RH, followed by gradual growth of the characteristic peak of Cu-krh at ~14°. Crystal structure of (b) Cu-src and (c) Cu-krh end-members. On hydration, water breaks the 3D Cu-src structure and acts as glue (H bonding) holding the 2D layers of Cu-krh. Grey (CuO_5 tetragonal pyramid, CuO_6 octahedra), cyan (Na atom), yellow shades (SO_4 tetrahedra), black (Cu1), pink (Cu2), red-brown (Cu3) and green (Cu4) are the legends used for structural illustration. In case of $Na_2Cu(SO_4)_2$, Cu1, Cu2, Cu3 and Cu4 are known to form distorted heptahedra CuO_7 having two oxygens at a longer distance than in the tetragonal pyramid.

The Cu-src $Na_2Cu(SO_4)_2$ belongs to the monoclinic crystal system having noncentrosymmetric space group $P2_1$. There are four symmetrically distinct Cu sites characterized by unusual coordination with O. Each Cu atom form CuO_5 tetragonal pyramid composed of regular CuO_4 square in the equatorial (eq) plane and an apical O at slightly larger distance than Cu-O_{eq} bond. Further, weaker (longer) bonds are accounted in the Cu polyhedra to satisfy its bond valence sum. The Cu1 and Cu4 atoms form a distorted octahedra i.e. tetragonal pyramid (CuO_5) combined with additional sixth O. On the other hand, Cu3 and Cu4 atoms are bound to two additional O forming heptahedral CuO_7 coordination.[13] In contrast, the Cu-krh has a pseudo layered framework made up of infinite octahedral-tetrahedral chains, formed by SO_4 tetrahedra

and $CuO_4(H_2O)_2$ octahedra, stacked along *c* axis. The chains are separated by Na^+ ion layers. Further, hydrogens (H1 and H2) of water molecule are attached to the two apex corners (O5) of the octahedral unit that are not shared with the SO_4 tetrahedra. The configuration results in two distinct H bonding (i) inter-layered H bond (O1-H1) and (ii) intra-layered H bond (H2-O4) which acts as glue imparting rigidity to the 2D framework. Due to the combined effect of H-bonding and attractive interaction between the electron cloud on oxygen (O5) and Na^+, the H_2O units are tilted away from each other. Clearly, the removal of structural H_2O unit can have cascading effect along inter and intra layered direction of kröhnkite framework. The structure of dehydrated product is further dictated by the type and size of metallic cation.[13] For instance, Co and Ni based anhydrous metallic bisulfate stabilize in same structure (s.g. *C*2/*c*, type II) with low octahedral MO_6 distortion. In comparison, the anhydrous analogue of Jahn-Teller (JT) active Cu^{2+} (r = 0.73 Å) and Mn^{2+} (r = 0.83 Å) based kröhnkite are completely different: namely saranchinaite-type $Na_2Cu(SO_4)_2$ (s.g. $P2_1$) and alluaudite-type $Na_{2+\delta}Mn_{2-\delta/2}(SO_4)_3$ (s.g. *C*2/*c*), respectively. In general, a pronounced JT distortion in the metal polyhedra results in significant lowering of crystal symmetry of the dehydrated product.

Phase stability. The thermodynamic driving force behind the phase stability and transformation behaviour between kröhnkite and saranchinaite was further investigated using room temperature acid calorimetry. The solution calorimetric data is summarised in Table 1. The enthalpies of dissolution (ΔH_{ds}) in 5N HCl at 25 °C are 4.65 ± 0.07 kJ/mol for Cu-src and 55.09 ± 0.63 kJ/mol for Cu-krh, indicating the hydrated $Na_2Cu(SO_4)_2$ (i.e. Cu-krh) has more endothermic heat of solution than the anhydrous $Na_2Cu(SO_4)_2$. The ΔH_{ds} of kröhnkite phase is consistent with previous report.[35]

Finally, the enthalpies of formation ($\Delta H°_f$) of Cu-src and Cu-krh from their constituent

binary sulfates, Na_2SO_4, and $CuSO_4$ (plus H_2O) were calculated using the thermochemical cycle in Table 2 and were found to be exothermic. The $\Delta H°_f$ of Cu-krh is −57.93 ± 0.86 kJ/mol and that of Cu-src is − 6.41 ± 0.59 kJ/mol, indicating that the hydrated $Na_2Cu(SO_4)_2$ is significantly more thermodynamically stable than the dehydrated $Na_2Cu(SO_4)_2$. The FTIR spectra for these two structures confirm more splitting for S−O bond in Cu-src compared to Cu-krh indicating the lower symmetry of SO_4^{2-} ion in dehydrated Cu-src structure (Fig. S3).

Table 3 also shows the thermochemical cycle used to determine the hydration enthalpy (ΔH_{hyd}) of Cu-src into Cu-krh. The ΔH_{hyd} equal to −51.52 ± 0.63 kJ/mol is strongly exothermic. The ΔH_{hyd} per mole of water is −25.76 ± 0.32 kJ/mol, consistent with the water molecule in $Na_2Cu(SO_4)_2{\cdot}2H_2O$ being strongly bound structural water. The strong exothermic enthalpy of hydration explains why Cu-src begins to transform into Cu-krh within 1.15 h at 70 % RH (as discussed in previous section).

Table 1 Calorimetric data for Cu-src $Na_2Cu(SO_4)_2$ and Cu-krh $Na_2Cu(SO_4)_2{\cdot}2H_2O$.

Composition	**ΔH_{ds} (kJ/mol)**	**$\Delta H°_f$ (kJ/mol)**
Na_2SO_4	20.65 ± 0.40 (6)[36]	
$CuSO_4$	−22.41 ± 0.44 (6)	
H_2O	−0.54[37]	
$Na_2Cu(SO_4)_2$	4.65 ± 0.07(6)	−6.41 ± 0.59
$Na_2Cu(SO_4)_2{\cdot}2H_2O$	55.09 ± 0.63 (5)	−57.93 ± 0.86

ΔH_{ds} is enthalpy of solution, $\Delta H°_f$ is enthalpy of formation from anhydrous binary sulfates (plus water). Errors are two standard deviations of the mean. Values in parentheses are the number of measurements.

Table 2 Thermochemical cycles for enthalpy of formation for $Na_2Cu(SO_4)_2$ and $Na_2Cu(SO_4)_2{\cdot}2H_2O$.

Cu-src [$Na_2Cu(SO_4)_2$]	***Enthalpy measurement***
$Na_2Cu(SO_4)_{2\ (s,\ 25\ °C)} + 4HCl_{\ (l,\ 25\ °C)} \rightarrow 2NaCl_{\ (sln,\ 25\ °C)} + CuCl_{2\ (sln,\ 25\ °C)} + 2H_2SO_{4\ (sln,\ 25\ °C)}$	$\Delta H_1 = \Delta H_{ds}\ (Na_2Cu(SO_4)_2$
$Na_2SO_{4\ (s,\ 25\ °C)} + 2HCl_{\ (l,\ 25\ °C)} \rightarrow 2NaCl_{\ (sln,\ 25\ °C)} + H_2SO_{4\ (sln,\ 25\ °C)}$	$\Delta H_2 = \Delta H_{ds}\ (Na_2SO_4)$
$CuSO_{4\ (s,\ 25\ °C)} + 2HCl_{\ (l,\ 25\ °C)} \rightarrow CuCl_{2\ (sln,\ 25\ °C)} + H_2SO_{4\ (sln,\ 25\ °C)}$	$\Delta H_3 = \Delta H_{ds}\ (CuSO_4)$
$Na_2SO_{4\ (s,\ 25\ °C)} + CuSO_{4\ (s,\ 25\ °C)} \rightarrow Na_2Cu(SO_4)_{2\ (s,\ 25\ °C)}$	$\Delta H_4 = \Delta H°_f(Na_2Cu(SO_4)_2) = -\Delta H_1 + \Delta H_2 + \Delta H_3$
Cu-krh [$Na_2Cu(SO_4)_2{\cdot}2H_2O$]	***Enthalpy measurement***
$Na_2Cu(SO_4)_2{\cdot}2H_2O_{\ (s,\ 25\ °C)} + 4HCl_{\ (l,\ 25\ °C)} \rightarrow 2NaCl_{\ (sln,\ 25\ °C)} + CuCl_{2\ (sln,\ 25\ °C)} + 2H_2O_{\ (sln,\ 25\ °C)} + 2H_2SO_{4\ (sln,\ 25\ °C)}$	$\Delta H_5 = \Delta H_{ds}\ (Na_2Cu(SO_4)_2{\cdot}2H_2O$
$H_2O_{\ (l,25\ °C)} \rightarrow H_2O_{\ (sln,\ 25\ °C)}$	$\Delta H_6 = \Delta H_{ds}\ (H_2O)$
$Na_2SO_{4\ (s,\ 25\ °C)} + CuSO_{4\ (s,\ 25\ °C)} + 2H_2O_{\ (l,25\ °C)} \rightarrow Na_2Cu(SO_4)_2{\cdot}2H_2O_{\ (s,\ 25\ °C)}$	$\Delta H_7 = \Delta H°_f\ (Na_2Cu(SO_4)_2\cdot 2H_2O = -\Delta H_5 + \Delta H_2 + \Delta H_3 + 2*\Delta H_6$
Hydration enthalpy of Cu-src [$Na_2Cu(SO_4)_2$]	
$Na_2Cu(SO_4)_{2\ (s,\ 25\ °C)} + 2H_2O_{\ (l,25\ °C)} \rightarrow Na_2Cu(SO_4)_2{\cdot}2H_2O_{\ (s,\ 25\ °C)}$	$\Delta H_{hyd} = \Delta H_8 = \Delta H_7 - \Delta H_4$

Table 3 Thermochemical cycles for enthalpy of formation for Cu-krh from hydrated binary sulfates.

Reactions	**Enthalpies (kJ/mol)**
$Cu_{\ (s,\ 25\ °C)} + S_{\ (s,\ 25\ °C)} + 2O_{2\ (g\ 25\ °C)} \rightarrow CuSO_{4\ (s,\ 25\ °C)}$	$\Delta H_9 = -771.4 \pm 1.3$ [a]
$2Na_{\ (s,\ 25\ °C)} + S_{\ (s,\ 25\ °C)} + 2O_{2\ (g,\ 25\ °C)} \rightarrow Na_2SO_{4\ (s,\ 25\ °C)}$	$\Delta H_{10} = -1387.8 \pm 0.4$ [a]
$H_{2\ (g,\ 25\ °C)} + 0.5O_{2\ (g,\ 25\ °C)} \rightarrow H_2O_{\ (l,\ 25\ °C)}$	$\Delta H_{11} = -285.83 \pm 0.1$ [a]
$Cu_{\ (s,\ 25\ °C)} + S_{\ (s,\ 25\ °C)} + 4.5O_{2\ (g\ 25\ °C)} + 5H_{2\ (g,\ 25\ °C)} \rightarrow CuSO_4.5H_2O_{\ (s,\ 25\ °C)}$	$\Delta H_{12} = -2279.7 \pm 3.4$ [a]
$2Na_{\ (s,\ 25\ °C)} + S_{\ (s,\ 25\ °C)} + 7.5O_{2\ (g,\ 25\ °C)} + 10H_{2\ (g,\ 25\ °C)} \rightarrow Na_2SO_4.10H_2O_{\ (s,\ 25\ °C)}$	$\Delta H_{13} = -4327.3 \pm 4.0$ [a]
$CuSO_{4\ (s,\ 25\ °C)} + 5H_2O_{\ (l,\ 25\ °C)} \rightarrow CuSO_4.5H_2O_{\ (s,\ 25\ °C)}$	$\Delta H_{14} = \Delta H_{hyd}\ (CuSO_4.5H_2O)$

	$= \Delta H_{12} - \Delta H_9 - 5*\Delta H_{11}$
	$= -79.15 \pm 3.6$
$Na_2SO_{4(s,\ 25\ °C)} + 10H_2O_{(l,\ 25\ °C)} \rightarrow Na_2SO_4.10H_2O_{(s,\ 25\ °C)}$	$\Delta H_{15} = \Delta H_{hyd}(Na_2SO_4.10H_2O)$
	$= \Delta H_{13} - \Delta H_{10} - 10*\Delta H_{11}$
	$= -\text{-}81.2 \pm 4.0$
$2Na_{(s,\ 25\ °C)} + Cu_{(s,\ 25\ °C)} + 2S_{(s,\ 25\ °C)} + 5O_{2\ (g,\ 25\ °C)} + 2H_{2\ (g,\ 25\ °C)} \rightarrow Na_2Cu(SO_4)_2 \cdot 2H_2O_{(s,\ 25\ °C)}$	$\Delta H_{16} = \Delta H_9 + \Delta H_{10} + 2*\Delta H_{11} + \Delta H_7$
	$= -2788.8 \pm 1.6$
$CuSO_4.5H_2O_{(s,\ 25\ °C)} + Na_2SO_4.10H_2O_{(s,\ 25\ °C)} \rightarrow Na_2Cu(SO_4)_2 \cdot 2H_2O_{(s,\ 25\ °C)} + 13H_2O_{(l,\ 25\ °C)}$	$\Delta H_{17} = \Delta H_{16} + 13*\Delta H_{11} - \Delta H_{12} - \Delta H_{13}$
	$= 102.4 \pm 5.5$

a = Robie, R.A. & Hemingway, B.S.[38]

The enthalpies of formation from dehydrated binary sulfates for the different phases studied are compared in Fig. 3. Both Cu-src and Cu-krh are energetically significantly metastable with respect to a mixture of hydrated binary sulfates. This mixture has significantly more waters of hydration than Cu-krh. Both Cu-src and Cu-krh were prepared by spray drying followed by annealing at higher temperature or via dissolution reprecipitation technique, involving minimal amounts of water. The calorimetric data strongly suggest that their synthesis in an abundant aqueous medium would be unfavorable, as the mixture of hydrated binary sulfates is clearly more stable, and any ternary phase initially formed could decompose and recrystallize as a mixture of hydrated copper sulfate and hydrated sodium sulfate.

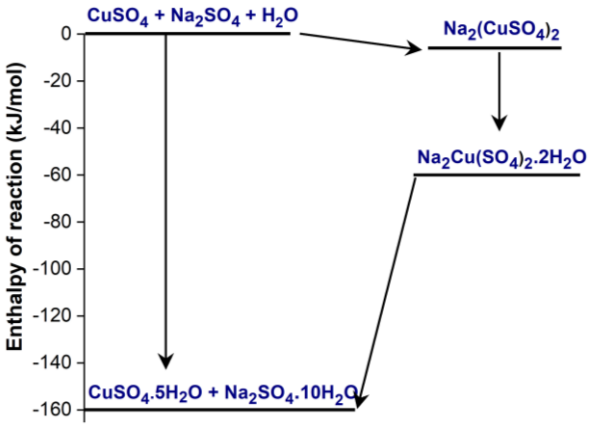

Fig. 3 Energy landscape depicting the enthalpies of the hydrated and dehydrated phases studied relative to a mixture of anhydrous binary sulfates plus water taken as the zero of enthalpy.

Alkali ion diffusion. The ionic diffusion in a material depends on the migration pathway offered by its crystalline lattice. Hence, the ionic conductivity of Cu-krh and Cu-src are expected to differ. The ionic conductivity was probed using AC impedance spectroscopy technique on compacted pellets. The AC impedance spectra of two materials are compared at 60 °C in Fig. 4(a). The Cu-src exhibits about 20 times higher impedance the Cu-krh at 60 °C. The values are ~ 9.6 $\times 10^{8}$ Ω.cm and ~ 5 × 10^{7} Ω.cm, respectively. The corresponding total conductivities are 1.04 × 10^{-9} S/cm (Cu-src) and 2 × 10^{-8} S/cm (Cu-krh). As shown in Fig. 4(b), at room temperature, the total ionic conductivity of Cu-krh is of the order of 10^{-8} S/cm, which is one order lower than the value of sulfate alluaudite $Na_{2.56}Fe_{1.72}(SO_4)_3$ (10^{-7} S/cm).[39]. In the temperature range of -35 °C to 60 °C, the total and electronic conductivities of Cu-krh is nearly of the same order (e.g. 2 × 10^{-8} S/cm vs. 1.13× 10^{-8} S/cm at 25 °C) and trace a parallel path. The quasi-stable current for the electronic conductivity was measured by potentiostatic polarization (Figure S4). The ionic transference number at 25 °C is estimated as $(\sigma_{total}-\sigma_e)/\ \sigma_{total}$= 43.5 %, suggesting that the total conduction is almost equally contributed by ionic and electronic transport in Cu-krh $Na_2Cu(SO_4)_2.2H_2O$. Such high contribution of electronic transport has been reported in

$LiFePO_4$[39] and Fe-krh $Na_2Fe(SO_4)_2.2H_2O$[40,41] based on polaronic conductivity. The Arrhenius equation: $\sigma = \sigma_0 exp\left(\frac{E_a}{kT}\right)$, was used to estimate the activation energy for alkali ion migration, where σ, E_a, k and T are ionic conductivity, activation energy, Boltzmann's constant, and absolute temperature respectively. From the plot of ln σ *vs.* $\frac{1000}{T}$, the slope can be found and multiplied with a factor of (1000*8.6173*10^{-5}) to find the activation energy (eV). The activation energy for ionic migration in Cu-krh is 171.2 meV in the temperature range of -20 °C to 40 °C. This value is significantly lower than ~1.16 eV calculated for Na^+-ion migration along most probable inter-layered [$01\bar{1}$] direction of Fe-krh.[40] The presence of defects such as V'_{Na}, Na'_{Fe} in Fe-krh synthesized under weak acidic condition ensures reduced migration energy (480 eV) augmented by interconnection of [$01\bar{1}$] diffusion pathways.[41] The highly distorted CuO_6 octahedra in Cu-krh may further activate such defects resulting in the facile migration of Na^+ ion.

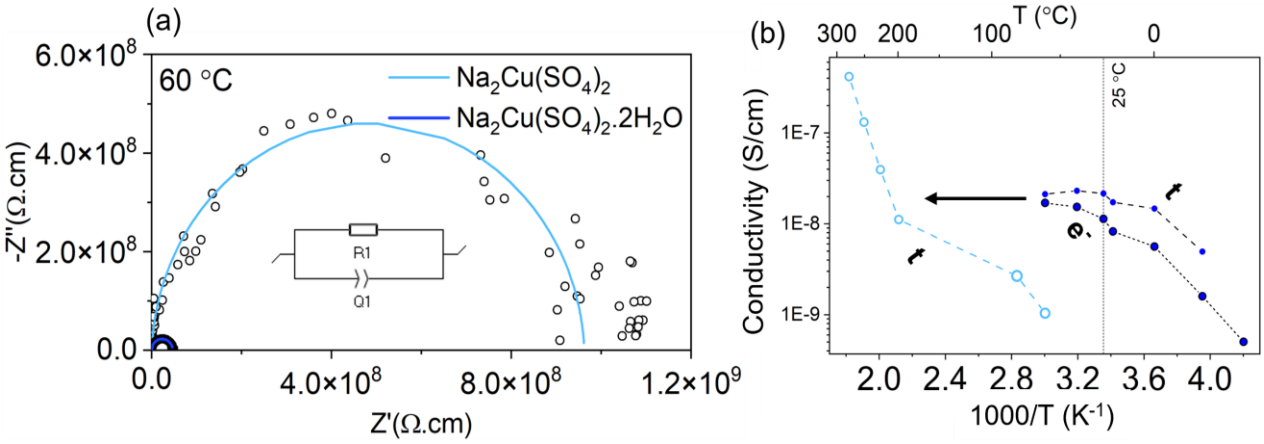

Fig. 4 Ionic conductivity (a) AC impedance spectra of Cu-krh and Cu-src at 60°C. The equivalent circuit in the inset having parallel combination of resistance R and constant phase element Q was used to fit the impedance spectrum. (b) The temperature dependent variation of total (t) and electronic (e^-) conductivity. For Cu-src, impedance spectra were not observed below 60 °C due to high data dispersion (noise). The dc polarization current was too low to be detected for Cu-src.

For Cu-src, the activation energy of Na^+ ion migration is 1.03 eV in the temperature range 200 to 277 °C, somewhat closer to the value of > 1.6 eV reported earlier based on bond valence sum energy calculations.[13] Further, there is a slight change in the slope below 80 °C. The high activation energy can be ascribed to the absence of interconnected diffusion channel in the Cu-src framework.[13] While the reason for the experimentally observed lower migration energy value is not fully understood, it can stem from the effects of highly distorted CuO_6 and CuO_7 polyhedra of Cu-src lattice on creation of cationic defects and its variation with temperature.

Electronic structure and insertion voltage prediction. The (de)insertion reaction in Cu-src compound is limited by the absence of open channel for alkali migration, high Cu^{2+}/Cu^{3+} redox potential and Jahn-Teller activity.[13] Thus, we have explored the hidden electronic structure property of $Na_2Cu(SO_4)_2$ system and predicted the (de)insertion voltage for removal of one Na from the framework with the help of DFT based first principles calculations. Fig. 5(a) represents the minimum energy configuration of optimized crystal structure for the fully sodiated phase containing sixteen Na atoms, whereas the half-desodiated phase has been depicted in Fig. 5(b), being reconstructed by symmetrically removing eight Na atoms. The atom projected density of states for both the phases, as illustrated in Fig. 5(c) and (d), represent the elemental orbital contribution of the constituent elements in the structure. It is observed that both the phases represent semi-metallic behavior in the up-spin channel with a band gap of 0.15 eV and 0.08 eV respectively. A closer look in the projected density of states reveals that near the Fermi level, the major contribution in the valence band arises from Cu-3*d* and O-2*p* orbital.

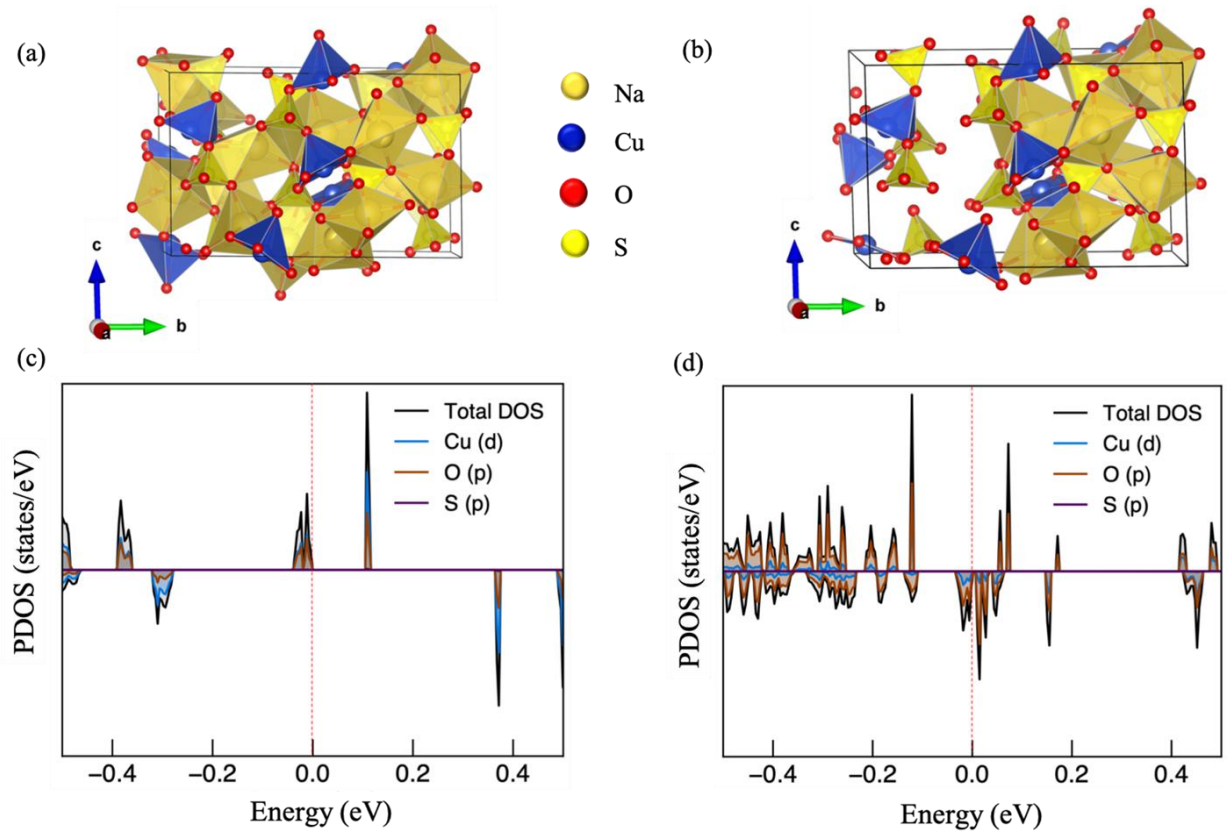

Fig. 5 (a-b) Optimised geometries and (c-d) density of states of full-sodiated and half-desodiated Cu-src system, respectively.

In the subsequent step, we have analyzed the redox potential for this system from the DFT calculated ground state energy. For the following half-desodiation reaction,

$$Na_2Cu(SO_4)_2 \leftrightarrow NaCu(SO_4)_2 + \Delta x\ (Na^+ + e)$$

the average redox potential can be expressed as:

$$\overline{V}\ (x_1, x_2) = \frac{[E_{Tot}\{Na_2Cu(SO_4)_2\} - E_{Tot}\{NaCu(SO_4)_2\} - \Delta x.\, E_{Na}]}{\Delta x.\, e}$$

where E_{Na} is the ground state energy of stable body center cubic Na metal per atom and Δx is the number of Na ions intercalated. In half desodiated reaction Δx equals to 1 while considering the intercalation limit $x_2 = 2$ and $x_1 = 1$ for full and half-desodiated phases. Using the above relation, we calculated the average intercalation voltage V(1,2) = 4.84 V in the half-desodiation process

(Na2 → Na1). Moreover, Bader charge analysis was performed to explore the charge transfer mechanism in the desodiation process. From the analysis, we have found that each of the Na atoms donate most of its electrons ($\Delta q > +0.8e$) indicating the ionic nature. Cu and S atoms also donate electrons whereas O atoms are the acceptors with negative Δq. Since our system contains a total of 104 and 96 atoms in full and half-desodiated phase, we have summarized the charges only on the Na atoms in Table S3.

Conversion Chemistry. Despite several attempts on cathode optimization, carbon coating and electrolyte formulation, no distinct Cu^{3+}/Cu^{2+} redox activity was observed at high-voltage as predicted by the DFT calculations. The high Cu^{3+}/Cu^{2+} redox potential combined with pronounced JT activity of Cu^{2+} (d^9) ion resulted in negligible (de)intercalation capacity marred with high irreversibility in Cu-bearing polyanionic sulfates. Such materials have been explored for extrusion and conversion chemistry in the lower voltage regime.[14,18–20] Thus, the electrochemical properties of Cu-src and Cu-krh compounds were evaluated upon reaction with Li/Na in the voltage range of 0.05 – 4 V. The galvanostatic (dis)charge profile of Cu-src in Li half-cell and Na half-cell are shown in Fig. 6a and Fig S6, respectively. The title compounds exhibit the first discharge capacity of 650 mAh/g and 240 mAh/g, characterized by electrochemical activity below 2V, respectively. Similar electrochemical behaviour is exhibited by Cu-krh (Fig. S7). Two important points are noted: (1) the capacity values were significantly higher than the theoretical values based on a two-electron reaction for a complete reduction of Cu^{2+} to Cu^0 i.e., 177.69 mAh/g and 158.73 mAh/g, respectively, and (2) the first discharge was followed by an irreversible capacity loss of 450 mAh/g (Cu-src vs. Li^+/Li), 90 mAh/g (Cu-src vs. Na^+/Na) and 550 mAh/g (Cu-krh vs. Li^+/Li). The first point ruled out the likelihood of a

displacement reaction. Alternatively, the electrochemical behavior is most likely based on a conversion reaction-based mechanism for Li uptake similar to the reported compounds like brochantite $Cu_4(OH)_6SO_4$ and jarosite $KFe_3(SO_4)_2(OH)_6$.[20,42] The lower capacity exhibited by $Na/Na_2Cu(SO_4)_2$ cell may be related to the larger size of Na^+ ions resulting in reduced mobility and formation of denser intermediate product such as Na_2O which is an electronic and ionic insulator.[47]

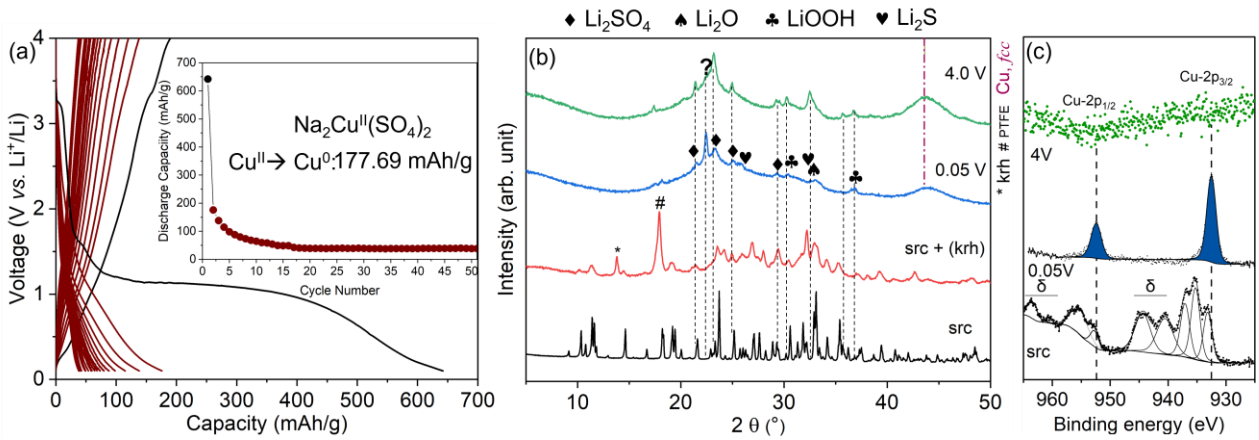

Fig. 6 (a) Galvanostatic profile of Cu-src $Na_2Cu(SO_4)_2$ acquired at a current rate of 2 mA/g using 1M $LiClO_4$-PC electrolyte and Li metal anode in half cell. Inset shows the cycling stability over 50 cycles with capacity retention of 40 mAh/g. The black and maroon line represent the first and subsequent cycles during galvanostatic cycling. *Post-mortem* analysis. (b) Ex situ XRD comparison of Cu-src cathode at pristine (black), discharged 0.05 V (blue) and charged 4.0 V (green) state. In the process of Spex milling of src with Super P Carbon slight hydration to Cu-krh (marked *) occurred as shown by the red line. The XRD peak of PTFE is marked by #. (c) Comparative ex situ XPS spectra of Cu-src and Cu-krh at the discharged (0.05 V, blue line) and charged (4 V, green line) state. The black and mustard yellow lines correspond to pristine Cu-src and Cu-krh electrode. The δ marked regions in XPS spectra of Cu-src represent satellite peaks.

Postmortem analysis was carried out by synergizing ex situ XRD and XPS techniques to confirm the conversion reaction mechanism for the Cu-src compound (Fig. 6b,c). In the electrode mixture of Cu-src and Super P Carbon, a small amount of Cu-krh (marked *) was noticed due to the ambient moisture sensitivity of Cu-src. To avoid the secondary phase, the electrode was heated overnight at 200 °C. The XRD pattern of the Cu-src electrode at 0.05 V indicated at

conversion reaction with complete decomposition of the pristine structure during Li uptake. The signature peaks related to Li_2SO_4, Li_2O, LiOH and Li_2S are assigned in the 2θ range of 20-40°. These phases can also contribute to the amorphous matrix. A broad peak at ~45° is correlated to the nanodomains of extruded metallic Cu(111),[43] which can become intense upon growth/ formation of Cu dendrites.[14,19] Subsequent charge to 4 V did not lead to pristine Cu-src phase. Further, the peaks corresponding to Li_2SO_4 intensified along with the broad Cu peak. Overall, it appears that Li_2SO_4/$LiNaSO_4$ is formed as an intermediate product accompanied with the structural breakdown of Cu-src $Na_2Cu(SO_4)_2$, expulsion of metallic Cu and an unknown product during the initial Li uptake. Subsequently, Li_2SO_4 reacts with eight mole Li forming one mole Li_2S and 4 mole Li_2O. On charging, the metallic Cu may catalyze the reversal of the above reaction resulting in the formation of Li_2SO_4.[42] However, as seen in the *ex situ* XRD plot the Cu metal doesn't revert to the matrix thus leading to large irreversibility.

XPS measurements were performed to track the oxidation state of Cu in Cu-src during the conversion reaction (Fig. 6c). For pristine Cu-src (Fig. 6c bottom) and Cu-krh (Fig. S8) electrodes, two or more peaks were noticed suggesting different types of Cu-O bonds viz. Cu-O-Cu (Cu-O-H) and Cu-O-S.[20] The presence of two unique Cu^{2+} polyhedra (CuO_6 and CuO_7) in Cu-src can further contribute to the peak broadness. The characteristic satellite peaks for Cu^{2+}, marked as δ, are present at higher binding energies. The deconvoluted peaks of Cu $2p_{3/2}$ at 933.14 eV, 935.26 eV and 937.06 eV can be assigned to CuO and $CuSO_4$ type contributions.[20] On lithiation to 0.05 V, the profile of the Cu-2p core peak shifted towards lower binding energy. The disappearance of satellite peaks suggests a decrease in the oxidation state of Cu from +2 to +1/0. The new Cu-$2p_{3/2}$ and Cu-$2p_{1/2}$ peaks were centered at 932.57 eV and 952.40 eV, respectively. Since the peak position of Cu-$2p_{3/2}$ is closer to 932.63 eV, it can be assigned to Cu

metal. However, there may be minor contributions from Cu_2O (932.18 eV) and Li-Cu interaction (931.1 eV).[20,44,45] On subsequent charge to 4 V, the signal from Cu-2p core was absent implying the irreversible nature of the conversion reaction of Cu-src on lithiation. The factors such as: (1) dissolution of Cu^+ species, formed on oxidation, in electrolyte, (2) migration of Cu^+ to Li metal anode during cycling, and (3) burying of Cu in the amorphous matrix of reaction products, may cause the absence of Cu-2p core signal from the electrode surface.[14,18,19,42,43,46]

This high irreversibility of the conversion reaction shown by polyanionic compounds can be overcome by enhancing the electronic conductivity by (1) increasing carbon content in the electrode mixture to help in the recovery of Cu^{2+} species,[43] and (2) nano-structuring the cathode compounds.[20,42] Overall, the *postmortem* analysis confirmed the conversion reaction mechanism exhibited by Cu-src on reaction with Li. It proceeds with the structural breakdown and expulsion of Cu metal in the matrix of Li_2S, Li_2O and Li_2SO_4. On oxidation, the Cu^{2+} species are not recovered which may be due to the dissolution of Cu^+, formed from Cu metal, in the electrolyte or its migration towards Li anode.

CONCLUSIONS

A scalable economic aqueous spray drying route has been employed to prepare monoclinic $Na_2Cu(SO_4)_2.xH_2O$ (x=0-1) bisulfate minerals. The hydrated kröhnkite $Na_2Cu(SO_4)_2.2H_2O$ has a pseudolayered 2D structure with water of hydration imparting rigidity along interlayered and intralayered direction based on H-bonding. High distortion in Jahn-Teller active Cu^{2+} polyhedra resulted in significant lowering of symmetry of the dehydrated saranchiante $Na_2Cu(SO_4)_2$ phase. The saranchinate can be quickly and reversibly hydrated with hydration involving shell-core model. On the phase stability landscape, kröhnkite is

thermodynamically stable than saranchinaite indicated by highly exothermic enthalpy of hydration (-51.51 ± 0.63 KJ/mol). However, with prolonged hydration, kröhnkite can decompose into $CuSO_4.5H_2O$ and $Na_2SO_4.10H_2O$. Due to open crystal structure, kröhnkite offers higher conductivity than saranchinaite. As per DFT calculation, saranchinaite can work as high voltage cathode (4.84 V vs Li^+/Li^0) involving both cationic (Cu^{2+}/Cu^{3+}) and anionic (O^-) redox activity. However, the combination of Jahn-Teller activite Cu^{2+} ion and constricted diffusion channel in saranchinaite make it difficult to realize the (de)insertion activity. On the other hand, these Cu-phases can work as electrode involving conversion reaction with high discharge capacity. However, irreversible capacity loss was noticed due to the formation of metallic Cu on lithiation and its dissolution in the electrolyte during the delithiation process. With due optimization leading to nanostructured electrode composite, these Cu-based polyanionic sulfates can work as potential battery electrodes involving conversion redox chemistry.

ASSOCIATED CONTENT

Supporting Information. The supporting information is available free of charge at the ACS publication website. Thermal analysis (TG-DSC) and XRD showing saranchinite phase evolution, Crystallographic details of kröhnkite $Na_2Cu(SO_4)_2.2H_2O$ and saranchinite $Na_2Cu(SO_4)_2$, FT-IR and UV-VIS-NIR spectra, Bader charge analysis, galvanostatic voltage profile of kröhnkite phase, XPS spectrum with Cu 2p peak (PDF).

AUTHOR INFORMATION

Corresponding Author

* E-mail: prabeer@iisc.ac.in, www.prabeer.org; Fax: +91 80 2360 7316.

ORCID:

Shashwat Singh: 0000-0002-4163-219X

Audric Neveu: 0000-0003-0321-1789

Kumar Jayanthi: 0000-0002-5016-3575

Tisita Das: 0000-0001-5212-5102

Sudip Chakraborty: 0000-0002-6765-2084

Alexandra Navrotsky: 0000-0002-3260-0364

Valerie Pralong: 0000-0003-4644-8006

Prabeer Barpanda: 0000-0003-0902-3690

CONFLICTS OF INTEREST

The authors declare no competing financial interest.

ACKNOWLEDGMENTS

The current work was financially supported by the Technology Mission Division (Department of Science and Technology, Govt. of India) under Materials for Energy Storage (MES-2018) program (DST/TMD/MES/2K18/207). SS thank the Ministry of Human Resource Development (MHRD) for financial support. SS, AN, VP and PB thank the Indo-French Laboratory of Solid State Chemistry (LAFICS) for financial support. AN and KJ acknowledge the financial support from the U.S. Department of Energy, Office of Basic Energy Sciences, Grant DE-SC0021987. TD and SC are grateful to HRI Allahabad and DST-SERB (SRG/2020/001707) for generous funding. Computational work was carried out at the cluster computing facility in the Harish-Chandra Research Institute. We acknowledge Prof. P.V. Kamath (Bangalore University)

for providing *in*-situ hydration XRD facility. PB is grateful to the Alexander von Humboldt Foundation (Bonn, Germany) for a Humboldt Fellowship for experienced researchers and Prof. Dr. Maximilian Fichtner for hosting him at HIU, Ulm, Germany.

NOTES AND REFERENCES

1 P. Barpanda, M. Ati, B. C. Melot, G. Rousse, J.-N. Chotard, M.-L. Doublet, M. T. Sougrati, S. A. Corr, J.-C. Jumas and J.-M. Tarascon, *Nat. Mater.*, 2011, **10**, 772–779.

2 O. Yakubovich, N. Khasanova and E. Antipov, *Minerals*, 2020, **10**, 524.

3 F. Hatert, in *Minerals as Advanced Materials II*, ed. S. V Krivovichev, Springer Berlin Heidelberg, Berlin, Heidelberg, 2011, pp. 279–291.

4 P. Barpanda, *Isr. J. Chem.*, 2015, **55**, 537–557.

5 P. Barpanda, G. Oyama, S. I. Nishimura, S. C. Chung and A. Yamada, *Nat. Commun.*, 2014, **5**, 1–8.

6 T. Balić-Žunic, A. Garavelli, P. Acquafredda, E. Leonardsen and S. P. Jakobsson, *Mineral. Mag.*, 2009, **73**, 51–57.

7 W. Ko, H. Park, J. H. Jo, Y. Lee, J. Kang, Y. H. Jung, T. Y. Jeon, S. T. Myung and J. Kim, *Nano Energy*, 2019, **66**, 104184.

8 P. Singh, K. Shiva, H. Celio and J. B. Goodenough, *Energy Environ. Sci.*, 2015, **8**, 3000–3005.

9 O. I. Siidra, E. A. Lukina, E. V. Nazarchuk, W. Depmeier, R. S. Bubnova, A. A. Agakhanov, E. Yu. Avdontseva, S. K. Filatov and V. M. Kovrugin, *Mineral. Mag.*, 2018, **82**, 257–274.

10 H. Ait Ousaleh, S. Sair, A. Zaki, A. Faik, J. Mirena Igartua and A. El Bouari, *Sol. Energy*, 2020, **201**, 846–856.

11 P. Barpanda, G. Oyama, C. D. Ling and A. Yamada, *Chem. Mater.*, 2014, **26**, 1297–1299.

12 M. Reynaud, G. Rousse, A. M. Abakumov, M. T. Sougrati, G. Van Tendeloo, J. N. Chotard and J. M. Tarascon, *J. Mater. Chem. A*, 2014, **2**, 2671–2680.

13 V. M. Kovrugin, D. O. Nekrasova, O. I. Siidra, O. Mentré, C. Masquelier, S. Y. Stefanovich and M. Colmont, *Cryst. Growth Des.*, 2019, **19**, 1233–1244.

14 M. Sun, G. Rousse, A. M. Abakumov, M. Saubanère, M. L. Doublet, J. Rodríguez-Carvajal, G. Van Tendeloo and J. M. Tarascon, *Chem. Mater.*, 2015, **27**, 3077–3087.

15 P. Poizot, S. Laruelle, S. Grugeon, L. Dupont and J. Tarascon, *Nature*, 2000, **407**, 496–499.

16 V. Bodenez, L. Dupont, M. Morcrette, C. Surcin, D. W. Murphy and J.-M. Tarascon, *Chem. Mater.*, 2006, **18**, 4278–4287.

17 A. Ponrouch, J. Cabana, R. Dugas, J. L. Slack and M. R. Palacín, *RSC Adv*, 2014, **4**, 35988–35996.

18 Y. Lee, C. H. Jo, J. K. Yoo, J. U. Choi, W. Ko, H. Park, J. H. Jo, D. O. Shin, S. T. Myung and J. Kim, *Energy Storage Mater.*, 2020, **24**, 458–466.

19 J. N. Schwieger, A. Kraytsberg and Y. Ein-Eli, *J. Power Sources*, 2011, **196**, 1461–1468.

20 R. Zhao, T. Yang, M. A. Miller and C. K. Chan, *Nano Lett.*, 2013, **13**, 6055–6063.

21 J. Kim, H. Kim and K. Kang, *Adv. Energy Mater.*, 2018, **8**, 1702646.

22 S. Singh, P. K. Jha, M. Avdeev, W. Zhang, K. Jayanthi, A. Navrotsky, H. N. Alshareef and P. Barpanda, *Chem. Mater.*, 2021, **33**, 6108–6119.

23 J. Rodríguez-Carvajal, *Phys. B Condens. Matter*, 1993, **192**, 55–69.

24 K. Momma and F. Izumi, *J. Appl. Crystallogr.*, 2011, **44**, 1272–1276.

25 M. V. Kilday, *J. Res. Natl. Bur. Stand.*, 1980, **85**, 467.

26 W. Kohn and L. J. Sham, *Phys. Rev.*, 1965, **140**, A1133–A1138.

27 P. E. Blöchl, *Phys. Rev. B*, 1994, **50**, 17953–17979.

28 G. Kresse and J. Furthmüller, *Phys. Rev. B*, 1996, **54**, 11169–11186.

29 J. P. Perdew, K. Burke and M. Ernzerhof, *Phys. Rev. Lett.*, 1996, **77**, 3865–3868.

30 H. J. Monkhorst and J. D. Pack, *Phys. Rev. B*, 1976, **13**, 5188–5192.

31 M. Reynaud, M. Ati, B. C. Melot, M. T. Sougrati, G. Rousse, J.-N. Chotard and J.-M. Tarascon, *Electrochem. Commun.*, 2012, **21**, 77–80.

32 L. Lander, M. Reynaud, G. Rousse, M. T. Sougrati, C. Laberty-Robert, R. J. Messinger, M. Deschamps and J. M. Tarascon, *Chem. Mater.*, 2014, **26**, 4178–4189.

33 O. I. Siidra, E. V. Nazarchuk, A. N. Zaitsev, E. A. Lukina, E. Y. Avdontseva, L. P. Vergasova, N. S. Vlasenko, S. K. Filatov, R. Turner and G. A. Karpov, *Eur. J. Mineral.*, 2017, **29**, 499–510.

34 Y. Meng, S. Zhang and C. Deng, *J. Mater. Chem. A*, 2015, **3**, 4484–4492.

35 J. Majzlan, D. Marinova and E. Dachs, *RSC Adv.*, 2020, **11**, 374–379.

36 P. Barman, D. Dwibedi, K. Jayanthi, S. S. Meena, S. Nagendran, A. Navrotsky and P. Barpanda, *J. Solid State Electrochem.* In Press.

37 V. B. Parker, *Natl. Bur. Stand.*, 1965, 66.

38 R. A. Robie and B. S. Hemingway, *Thermodynamic properties of minerals and related substances at 298.15 K and 1 bar (105 Pascals) pressure and at higher temperatures*, US Government Printing Office, 1995.

39 J. Lu and A. Yamada, *ChemElectroChem*, 2016, **3**, 902–905.

40 T. Watcharatharapong, J. T-Thienprasert, P. Barpanda, R. Ahuja and S. Chakraborty, *J Mater Chem A*, 2017, **5**, 21726–21739.

41 T. Watcharatharapong, J. T-Thienprasert, S. Chakraborty and R. Ahuja, *Nano Energy*, 2019, **55**, 123–134.

42 Y. L. Ding, Y. Wen, C. C. Chen, P. A. Van Aken, J. Maier and Y. Yu, *ACS Appl. Mater. Interfaces*, 2015, **7**, 10518–10524.

43 G. Parzych, D. Mikhailova, S. Oswald, J. Eckert and H. Ehrenberg, *J. Electrochem. Soc.*, 2011, **158**, A898.

44 M. C. Biesinger, *Surf. Interface Anal.*, 2017, **49**, 1325–1334.

45 M. C. Biesinger, L. W. M. Lau, A. R. Gerson and R. S. C. Smart, *Appl. Surf. Sci.*, 2010, **257**, 887–898.

46 L. Martin, H. Martinez, D. Poinot, B. Pecquenard and F. Le Cras, *J. Phys. Chem. C*, 2013, **117**, 4421–4430.

47 M. H. Rahman, A. M. Glushenkov, T. Ramireddy and C. Yeng, *Chem. Commun.*, 2014, **50**, 5057-5060.

Supplementary Information

Facile Synthesis and Phase Stability of Cu-based $Na_2Cu(SO_4)_2.xH_2O$ (x = 0-2) Sulfate Minerals as Conversion type Battery Electrodes

Shashwat Singh,†# Audric Neveu,# K. Jayanthi,$ Tisita Das,‡ Sudip Chakraborty,‡ Alexandra Navrotsky,$ Valérie Pralong,# and Prabeer Barpanda†§*

† Faraday Materials Laboratory (FaMaL), Materials Research Center, Indian Institute of Science, Bangalore 560012, India

Normandie University, ENSICAEN, UNICAEN, CNRS, CRISMAT, 14000 Caen, France

$ School of Molecular Sciences and Navrotsky Eyring Center for Materials of the Universe, Arizona State University, Tempe, Arizona 85287, United States

‡ Materials Theory for Energy Scavenging (MATES) Lab, Harish-Chandra Research Institute (HRI), HBNI, Chhatnag Road, Jhunsi, Prayagraj 211019, India

§ Helmholtz Institute Ulm (HIU), Helmholtzstraße, Ulm 89081, Germany

Corresponding Author

*E-mail: prabeer@iisc.ac.in

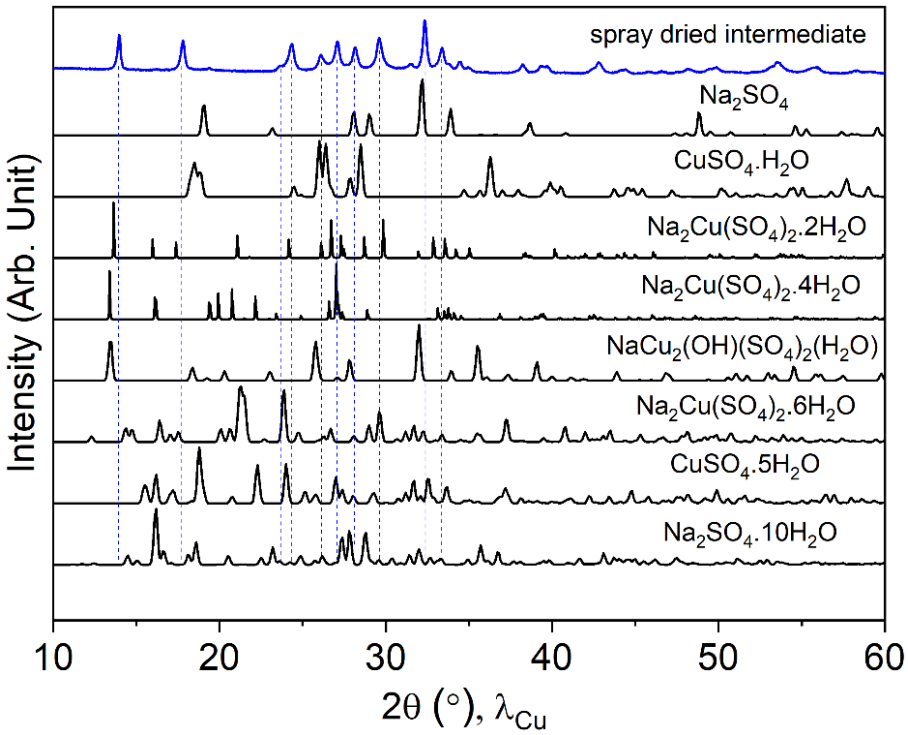

Fig. S7 PXRD pattern of the spray dried intermediate complex powder (blue line) is compared with the reference patterns of hydrated compounds $Na_2Cu(SO_4)_2.xH_2O$ (x = 2, 4 and 6), natrochalcite $NaCu_2(SO_4)_2(OH).H_2O$ and precursors $CuSO_4.5H_2O$, $CuSO_4.H_2O$, $Na_2SO_4.10H_2O$ and Na_2SO_4.

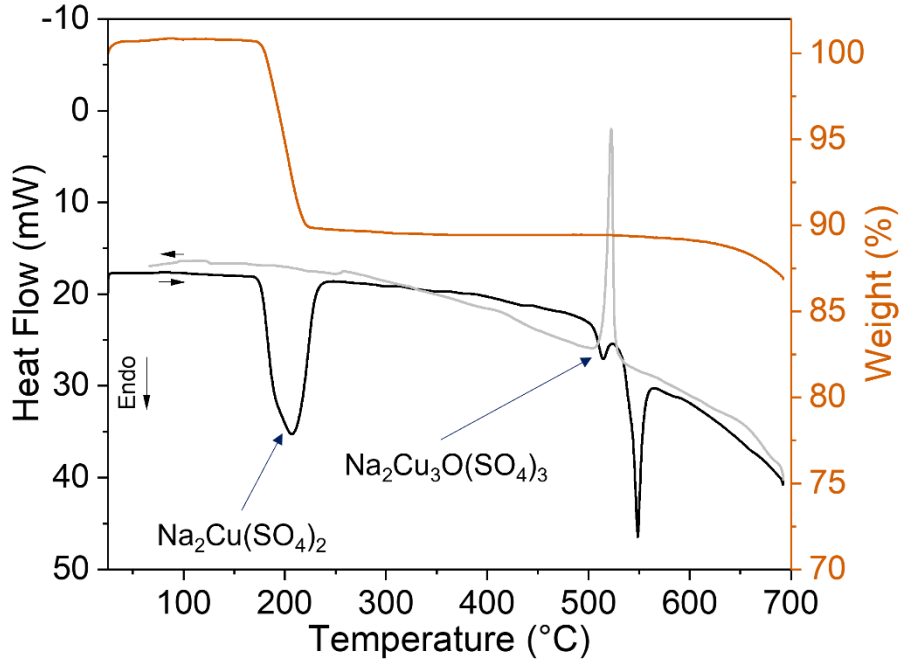

Fig. S8 Simultaneous thermal analysis (thermogravimetric and differential scanning calorimetry) plot for spray dried intermediate complex powder. The data was acquired at a heating rate of 10

°C/min in N_2 gas flow (50 mL/min). The grey line indicates the DSC curve acquired during cooling.

Table S1 Lattice and atomic parameters of kröhnkite $Na_2Cu(SO_4)_2.2H_2O$ determined from Rietveld refinement.

Formula [Molecular weight]	**$Na_2Cu(SO_4)_2.2H_2O$ [337.68]**
Crystal system	Monoclinic
Space group	$P\,2_1/c$ (#14), Z = 2
Unit cell parameter (Å)	a = 5.8078(1), b = 12.6664(0), c = 5.5173(4) β = 108.44
Unit cell volume (Å^3)	385.02(3)
Theoretical density (gcm^{-3})	2.9128
Reliability factors & goodness of fit values	Rp = 9.82 %, Rwp = 8.81 %, χ^2 = 11.3

Atom	Site	x	y	z	Occupancy	U_{iso}
Na	4e	0.5744	0.1253	0.2109	1	0.0003
Cu	2a	0	0	0	1	0.0003
S	4e	0.2371	0.1198	0.5428	1	0.0003
O1	4e	0.0108	0.1736	0.4907	1	0.0003
O2	4e	0.3004	0.0577	0.7796	1	0.0003
O3	4e	0.2328	0.0481	0.3391	1	0.0003
O4	4e	0.4456	0.1940	0.5635	1	0.0003
O5	4e	0.8374	0.1366	0.9497	1	0.0003
H1	4e	0.8976	0.1859	0.9680	1	0.0003
H2	4e	0.7120	0.1400	0.7900	1	0.0003

Table S2 Lattice and atomic parameters of saranchinaite $Na_2Cu(SO_4)_2$ determined from Rietveld refinement.

Formula [Molecular weight]	**$Na_2Cu(SO_4)_2$ [301.65]**
Crystal system	Monoclinic
Space group	$P\,2_1$ (#4), Z =8
Unit cell parameter (Å)	a = 8.9672(9), b = 15.5408(0), c = 10.1401(0) β = 107.087
Unit cell volume (Å^3)	1350.74
Theoretical density (gcm^{-3})	2.9667
Reliability factors & goodness of fit values	Rp = 14.3 %, Rwp = 14.6 %, χ^2 = 21.25

Atom	Site	x	y	z	Occupancy	U_{iso}
Na1	2a	0.28374	0.42257	0.05243	1	0.0003
Na2	2a	0.28937	0.41204	0.61718	1	0.0003
Na3	2a	0.97519	0.68519	0.24565	1	0.0003
Na4	2a	0.61794	0.54975	0.66348	1	0.0003
Na5	2a	0.36251	0.80324	0.41809	1	0.0004
Na6	2a	0.60322	0.58649	0.08643	1	0.0003
Na7	2a	0.93999	0.72662	0.66951	1	0.0003
Na8	2a	0.62924	0.26826	0.15688	1	0.0002
Cu1	2a	0.65082	0.07897	0.67666	1	0.0002
Cu2	2a	0.92753	0.31663	0.01380	1	0.0001
Cu3	2a	0.90613	0.53165	0.96179	1	0.0002
Cu4	2a	0.90104	0.53194	0.48433	1	0.0002
O1	2a	0.87930	0.05876	0.03320	1	0.0002
O2	2a	0.00950	0.36789	0.23260	1	0.0002
O3	2a	0.96460	0.41646	0.91060	1	0.0002
O4	2a	0.85550	0.64283	0.02120	1	0.0002
O5	2a	0.50010	0.67831	0.38250	1	0.0002
O6	2a	0.84960	0.79062	0.95450	1	0.0002
O7	2a	0.69060	0.50090	0.91580	1	0.0003
O8	2a	0.61240	0.71596	0.93700	1	0.0003
O9	2a	0.88390	0.47591	0.68250	1	0.0003
O10	2a	0.71580	0.67068	0.28010	1	0.0003
O11	2a	0.73580	0.21729	0.37890	1	0.0003
O12	2a	0.74370	0.61348	0.50660	1	0.0002

O13	2a	0.71220	0.34973	0.98610	1	0.0002
O14	2a	0.50910	0.01872	0.74650	1	0.0002
O15	2a	0.21090	0.47467	0.27310	1	0.0002
O16	2a	0.05710	0.45993	0.43170	1	0.0002
O17	2a	0.90050	0.32126	0.71640	1	0.0003
O18	2a	0.94100	0.11454	0.43230	1	0.0002
O19	2a	0.79440	0.14012	0.59220	1	0.0002
O20	2a	0.55720	0.39300	0.75650	1	0.0003
O21	2a	0.13590	0.40572	0.76670	1	0.0003
O22	2a	0.64360	0.13436	0.01570	1	0.0003
O23	2a	0.79190	0.16699	0.85730	1	0.0002
O24	2a	0.76060	0.67814	0.78100	1	0.0003
O25	2a	0.48680	-0.13490	0.73140	1	0.0003
O26	2a	0.88610	0.20960	0.09590	1	0.0002
O27	2a	0.47780	0.42807	0.95780	1	0.0004
O28	2a	0.72610	0.76692	0.46900	1	0.0003
O29	2a	0.46640	-0.05170	0.52530	1	0.0003
O30	2a	0.26130	-0.04830	0.63560	1	0.0003
O31	2a	0.94220	0.51881	0.20350	1	0.0002
O32	2a	0.66990	0.06576	0.38080	1	0.0003
S1	2a	0.56747	0.41358	0.89123	1	0.0001
S2	2a	0.74208	0.71073	0.92625	1	0.0001
S3	2a	0.06562	0.43822	0.30261	1	0.0001
S4	2a	0.66852	0.69608	0.39968	1	0.0001
S5	2a	0.75860	0.14268	0.42532	1	0.0002
S6	2a	0.97682	0.40069	0.74203	1	0.0002
S7	2a	0.42819	-0.06170	0.65153	1	0.0002
S8	2a	0.78464	0.14354	1.00114	1	0.0001

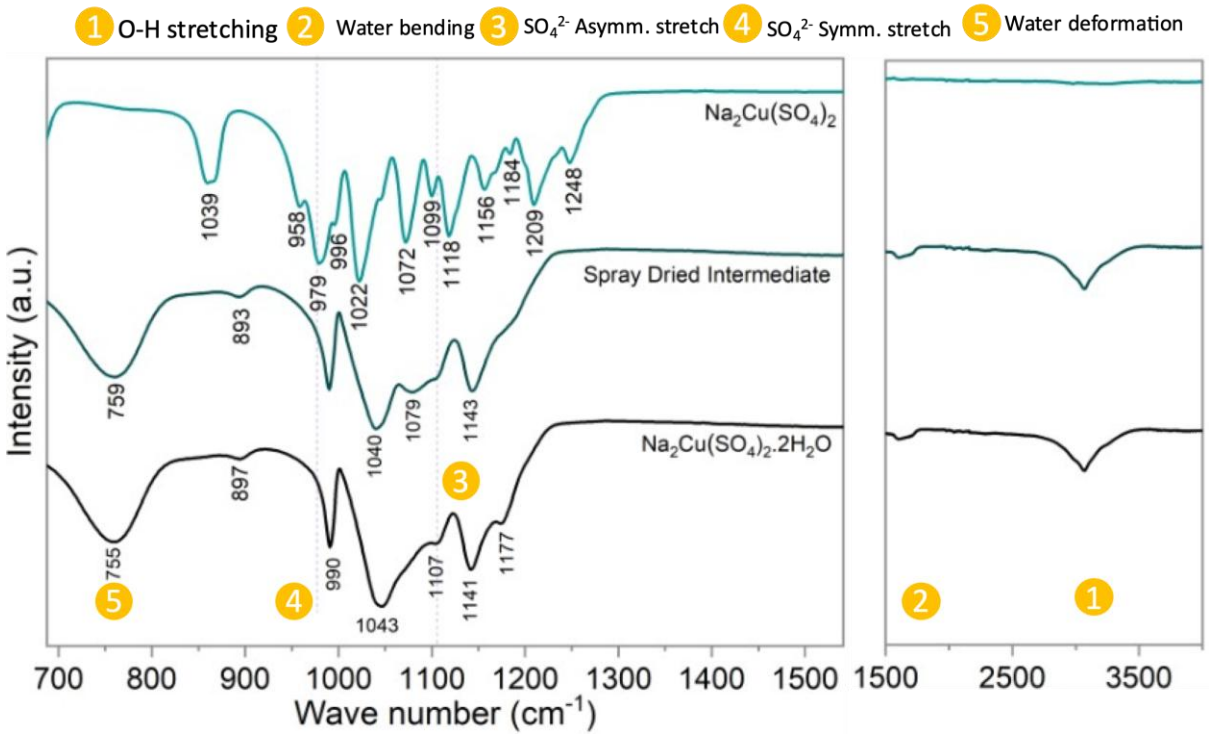

Fig. S9 FTIR spectra, acquired in ATR mode, of the Cu-krh, src and spray dried intermediate powder. The spectra of Cu-krh and spray dried intermediate powder are quite similar. However, the XRD patterns, as shown in figure 1, are different.

Table S3. Bader charge analysis during removal of one sodium from src $Na_2Cu(SO_4)_2$.

Atoms in full-sodiated phase	Bader Charge (Δq)	Atoms in half-desodiated phase	Bader charge (Δq)
Na1			
Na2	+0.8568	Na2	+0.8657
Na3	+0.8526	-	
Na4	+0.8526	Na4	+0.8578
Na5	+0.8461	Na5	+0.8461
Na6	+0.8461	-	
Na7	+0.8551	Na7	+0.8549
Na8	+0.8551	-	
Na9	+0.8639	Na9	+0.8638
Na10	+0.8639	-	
Na11	+0.8502	Na11	+0.8529
Na12	+0.8502	-	
Na13	+0.8483	Na13	+0.8490
Na14	+0.8483	-	
Na15	+0.8431	-	
Na16	+0.8431	Na16	+0.8459

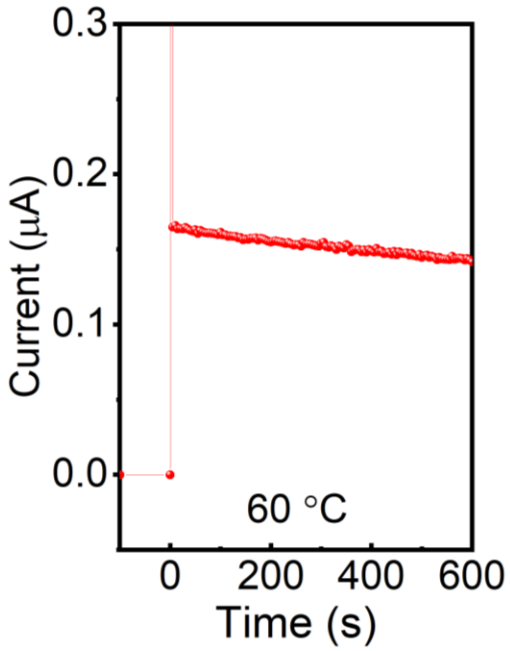

Fig. S10 The current response of Cu-krh acquired during potentiostatic polarization under an applied potential step of 2V at 60 °C.

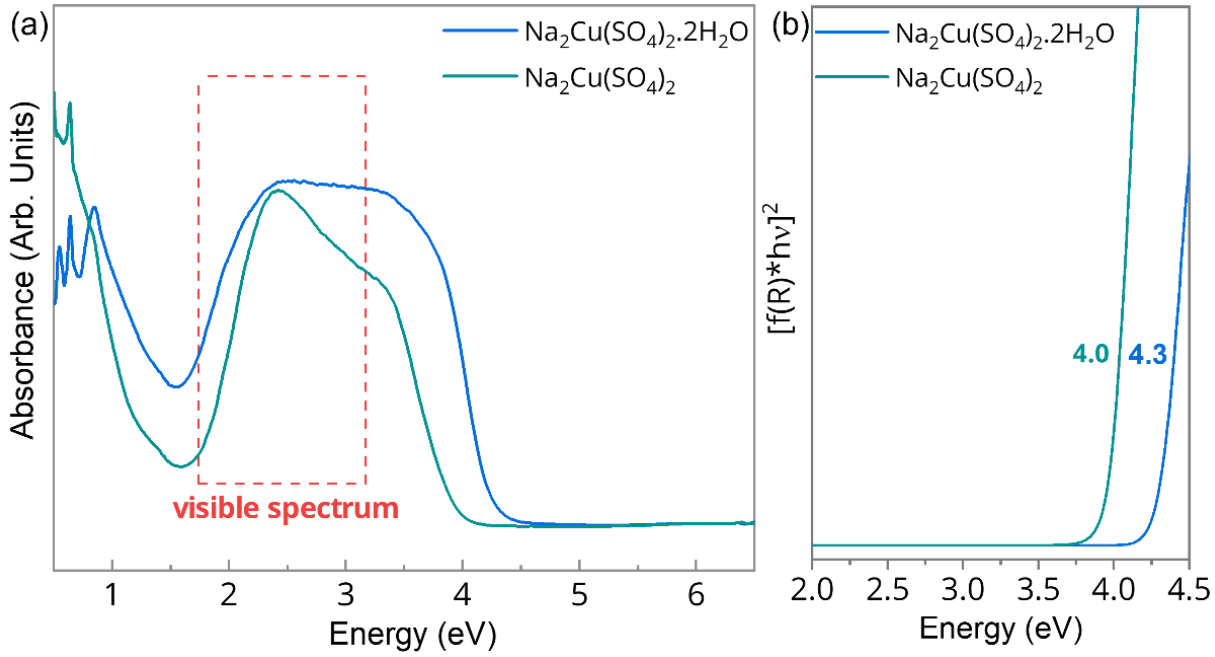

Fig. S11 (a) UV-VIS-NIR absorption spectra of the src and Cu-krh compounds, and (b) Optical band gap for the src and Cu-krh calculated using Kubelka-Munk function (n =2) applied to UV-VIS-NIR spectra

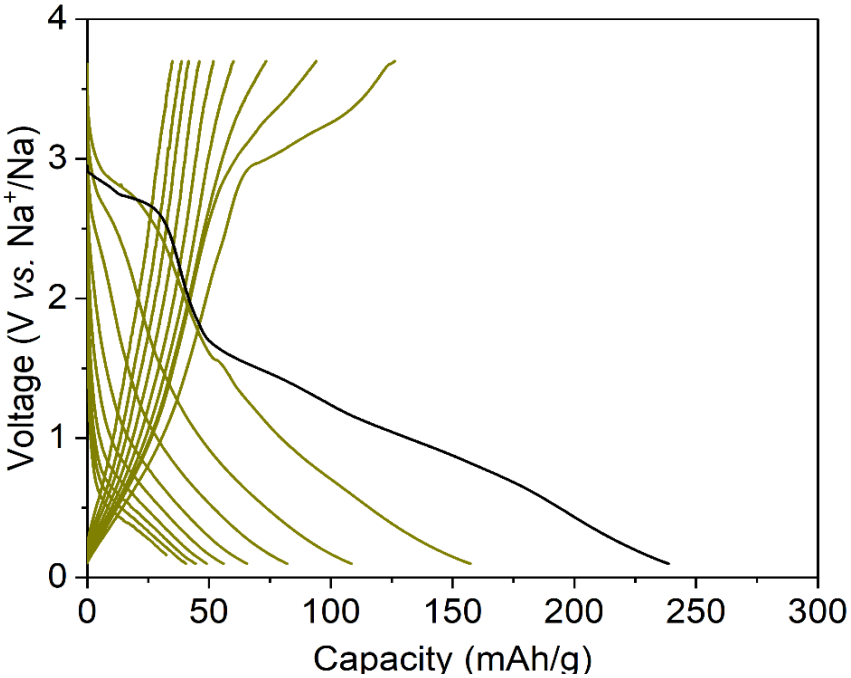

Fig. S12 Galvanostatic profile of Cu-src $Na_2Cu(SO_4)_2$ acquired at a current rate of 2 mA/g using 1M $NaPF_6$- EC/DEC electrolyte and Na metal anode in half cell. The black and dark yellow color represent the first and subsequent cycles during the galvanostatic cycling**.**

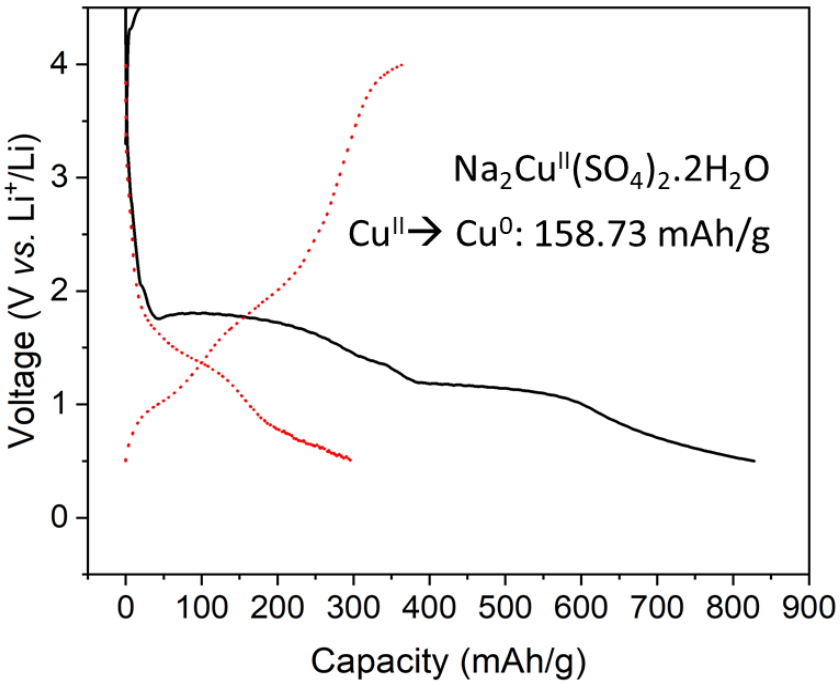

Fig. S7 Galvanostatic profile of Cu-krh $Na_2Cu(SO_4)_2.2H_2O$ acquired at a current rate of 2 mA/g using 1M $LiClO_4$-PC electrolyte and Li metal anode in half cell. The black and red line represent the first and second cycle during the galvanostatic cycling**.** A different galvanostatic profile of Cu-krh from src may stem from different structure and the water of hydration[1]. The in-depth mechanistic understanding will be pursued in future.

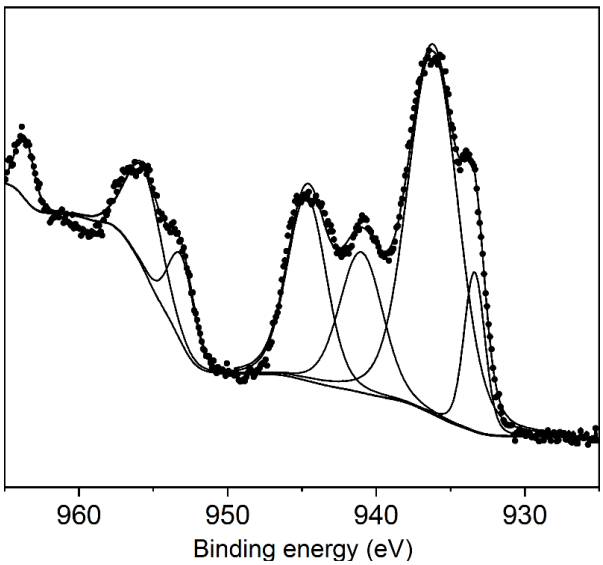

Fig. S8 XPS spectrum of Cu 2p core peak for pristine Cu-krh electrode. The characteristic satellite peaks of Cu^{2+} can be seen at the binding energies: 941.01 eV, 944.68 eV and 963.65 eV.

References

1. Schwieger, J. N.; Kraytsberg, A.; Ein-Eli, Y. Copper Sulfates as Cathode Materials for Li Batteries. *J. Power Sources* **2011**, *196* (3), 1461–1468. https://doi.org/10.1016/j.jpowsour.2010.07.090.